A Modeling Study of the Three-Dimensional Continental Shelf Circulation off Oregon. Part II: Dynamical Analysis

PETER R. OKE,* J. S. ALLEN, R. N. MILLER, AND G. D. EGBERT

College of Oceanic and Atmospheric Sciences, Oregon State University, Corvallis, Oregon

(Manuscript received 9 May 2001, in final form 19 September 2001)

ABSTRACT

Sixty-day simulations of the subinertial continental shelf circulation off Oregon are performed for a hindcast study of summer 1999. In Part I, the model results are shown to compare favorably with in situ currents and hydrographic measurements obtained from an array of moored instruments and field surveys and high-frequency radar–derived surface currents. In this paper, the modeled three-dimensional, time-varying circulation and dynamical balances are analyzed, providing a detailed synoptic description of the continental shelf circulation off Oregon for summer 1999. The circulation is clearly wind driven and strongly influenced by alongshore variations in shelf topography. In the region of the coast where the alongshore topographic variations are small the upwelling circulation is consistent with standard conceptual models for two-dimensional across-shore circulation. In the regions where the alongshore topographic variations are greater, the upwelling circulation is highly three-dimensional. Over Heceta Bank the upwelling circulation is complicated, with weaker direct coupling to the wind forcing over most of the shelf. It is demonstrated that the upwelled water that is found over the midshelf off Newport is upwelled to the north and is advected to the south. Additionally, upwelled water over Heceta Bank is drawn from a different location to the south. The dynamical balances over the inner shelf are divided into two regimes; in the coastal jet and inshore of the coastal jet. In the coastal jet the tendency of the alongshore depth-averaged velocity V_t is large and is driven by the difference between the surface and bottom stresses during upwelling. Inshore of the coastal jet, V_t is small and is driven by the difference between the surface stress and a negative alongshore pressure gradient during upwelling. When the wind stress becomes small after upwelling, V_t is primarily balanced by the negative alongshore pressure gradient and a northward flow is generated. Subsequently, the alongshore pressure gradient decreases, the flow becomes geostrophic, and the northward flow persists until the next significant event. A region to the south of Newport over the inner shelf is identified as the region where the northward momentum is initially generated.

1. Introduction

A modeling study of the coastal ocean circulation off Oregon during the 1999 upwelling season is presented. In Part I of this study (Oke et al. 2002b) model results are compared with in situ velocity, temperature, and salinity measurements and high-frequency radar–derived surface currents obtained during the summer of 1999 as a part of the Oregon State University (OSU) National Oceanographic Partnership Program (NOPP) project. A series of sensitivity experiments designed to assess the model's sensitivity to initial stratification, surface forcing, domain size, and river forcing demonstrate that surface heating is important, and that the model results are sensitive to initial stratification. The model configuration that compares most favorably with observed velocity and hydrographic fields is identified by comparing the model's skill, based on mean-squared error statistics, relative to a basic test case. The best model results are obtained from a simulation with time-varying, spatially uniform wind stress and with time varying surface heat. Three-dimensional, time-varying fields from this simulation are investigated in detail in this manuscript.

One of the aims of this study is to provide a complete synoptic description of the three-dimensional, time-varying continental shelf circulation off Oregon for summer 1999. We also aim to determine where the upwelled water comes from during wind-driven upwelling, and to determine to what extent the wind-driven upwelling circulation is two-dimensional in the across-shore plane as assumed in standard conceptual models (e.g., Allen et al. 1995). These aims are addressed by analyzing the time evolution of modeled fields during a strong upwelling event, and by performing an empirical orthogonal functions (EOF) analysis of modeled fields for the entire 60-day simulation.

* Current affiliation: School of Mathematics, University of New South Wales, Sydney, New South Wales, Australia.

Corresponding author address: Dr. Peter R. Oke, School of Mathematics, University of New South Wales, Sydney, NSW 2052, Australia.
E-mail: petero@maths.unsw.edu.au

We also aim to better understand the dynamical balances that prevail during upwelling, relaxation from upwelling, and during the generation of the northward flow over the innershelf off Newport that is commonly observed after strong upwelling events (e.g., Kundu and Allen 1976; Stevenson et al. 1974). The above-mentioned processes of interest are all time-dependent. Results from observations made during the Coastal Upwelling Experiments, CUE-I and CUE-II, show that while the mean alongshore current is baroclinic, dominant fluctuations of the alongshore currents in the vicinity of Newport (44.65°N) and Cascade Head (45.05°N) are nearly barotropic (Smith 1974; Kundu and Allen 1976). We therefore address the aims outlined above by performing an EOF analysis of the modeled dynamical balances in the depth-averaged alongshore momentum equation. Additionally, we analyze time series of these balances from fixed locations in space in order to isolate the dominant processes that govern the reversal of the alongshore currents after strong upwelling favorable winds.

The dynamics that govern the generation of a northward flow over the inner-shelf after upwelling in the region of the Coastal Ocean Dynamics Experiment (CODE) off California is investigated by Gan and Allen (2002). The alongshore variations in shelf topography in the CODE region are strongly related to the presence of headlands. Gan and Allen (2002) show that an alongshore pressure gradient that is set up by the interactions of the wind-driven flow with topography drives northward currents when the wind becomes weak. The alongshore variations in topography off central Oregon are mainly due to the presence of Heceta Bank. The continental shelf width broadens by greater than 40 km between Cascade Head (45.05°N) and Heceta Bank (44.05°N) over approximately 100 km in the alongshore direction. The qualitative consistencies between the reversals associated with wind relaxation off California and Oregon suggest that equivalent dynamics are likely to govern the reversals in both regions. However, the difference in the nature of the alongshore variations in topography that are important in both regions naturally leads to questions concerning the equivalence of the dominant dynamics in these regions. Flow reversals after upwelling events appear to be a robust feature of the upwelling circulation off the U.S. west coast, so it is important to understand the dynamics in different regions.

The outline of this paper is as follows. A description of the model configuration is presented in section 2 followed by a representative set of the model–data comparisons in section 3. An analysis of the three-dimensional modeled circulation and dynamical balances are given in section 4, followed by a summary in section 5.

2. Model configuration

The Princeton Ocean Model (POM: Blumberg and Mellor 1987) is configured for the Oregon continental shelf. The model grid (Fig. 1) extends 220 km offshore and 365 km in the alongshore direction. The maximum horizontal grid resolution is 2 km over the shelf in the vicinity of Newport, with decreased resolution toward the offshore and alongshore boundaries. The grid is rectangular and the axes have been rotated to 7°N in order to better align with the coastline. The horizontal velocity $\mathbf{v}$ has components (u, v) corresponding to the across-shore and alongshore velocities [depth averages denoted by $\mathbf{V}$ and (U, V)] in the (x, y) directions, so that u is positive onshore and v is positive toward the north. The vertical grid consists of 31 sigma levels, with 8 levels concentrated near the surface, and 4 near the bottom in order to resolve the respective boundary layers.

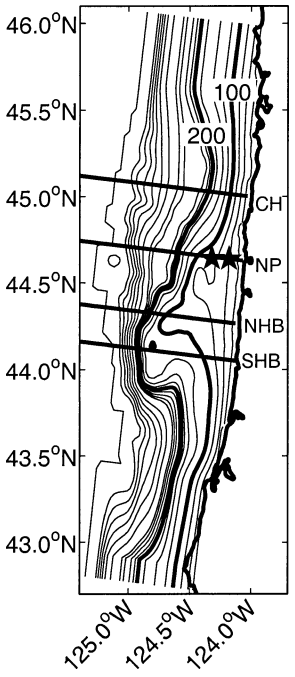

FIG. 1. Model topography (contour interval is 25 m for $H < 300$ m and 100 m for $H > 300$ m; 100- and 200-m isobaths are bold) showing the mooring locations (⋆) and the across-shore sections off Cascade Head (CH), Newport (NP), North Heceta Bank (NHB), and South Heceta Bank (SHB) that are referred to throughout the manuscript.

The model topography (Fig. 1) is linearly interpolated from a 1-km resolution dataset and smoothed to reduce the effects of pressure gradient errors due to the sigma coordinates. The minimum depth is 10 m. The maximum depth is set to 1000 m in order to reduce the constraint on the time steps that are 6 and 180 s for the barotropic and baroclinic modes, respectively. The vertical and horizontal viscosity (and diffusion) coefficients are flow-dependent according to the level-2.5 turbulence closure model of Mellor and Yamada (1982) and the formulation of Smagorinsky (1963), respectively. The horizontal diffusion coefficients are small (typically <10 m^2 s^{-1}) throughout the experiment considered in this study.

The alongshore boundary conditions are periodic for all variables. Consistent with this condition, an f-plane approximation is used, with $f = 1.037 \times 10^{-4}$ s^{-1}. In addition, an across-shore topographic section near the southern extent of the domain is interpolated over 10 alongshore grid cells to match an across-shore section near the northern extent of the domain, so that the topography is periodic in the y direction. The use of periodic boundary conditions establishes a well-posed and robust model, but is a limiting feature of this configuration. The most limiting aspect is the model's inability to represent net alongshore pressure gradients that might result from large scale, alongshore gradients in elevation or density. Additionally, periodic boundary conditions require the modeled flow at the northern and southern extent of the domain to be equal. Clearly, this is inconsistent with conditions in the real ocean. Despite these limitations, we find that this configuration is capable of reproducing a substantial fraction of the observed variance of the horizontal velocity field in the vicinity of Newport (Part I).

The offshore boundary conditions are zero gradient for the tangential velocities and elevation η, a modified radiation condition for the normal velocities (e.g., Chapman 1985), and an upstream advection condition for the potential temperature θ and salinity S. The horizontal diffusion coefficient is increased smoothly over five grid cells adjacent to the offshore boundary to a maximum of 1000 m^2 s^{-1} at the boundary in order to damp out unwanted reflection.

The alongshore component of the applied wind stress τ^{Sy} is calculated from time-varying winds measured at Newport and is assumed to be spatially uniform. To reduce the excitation of inertial oscillations the wind is low-pass filtered with a 40-h half-amplitude filter. The applied surface heat flux is calculated using observed meteorological variables and includes a feedback term between the observed air temperature and the modeled ocean surface temperature. Details of the heat flux formulation are presented in Part I of this study.

The initial fields of θ and S are horizontally uniform and the initial velocity fields are zero. The initial hydrographic profile is the mean observed offshore profile during CUE-II off Newport with the pycnocline raised by 20 m in order to better match with hydrographic observations during summer 1999. The model fields are spun up over 10 days with 5 days of constant 0.1 Pa, upwelling favorable winds followed by 5 days of no wind. This spinup allows the pycnocline to be upwelled to the surface and then relax to a quasi-equilibrium position. Across-shore sections off Cascade Head (CH), Newport (NP), northern Heceta Bank (NHB), and southern Heceta Bank (SHB) (denoted in Fig. 1) of v and potential density σ_θ at the end of the spin-up period are shown in Fig. 2. The fields of v at the end of the spinup period have a baroclinic southward coastal jet with maximum current magnitudes of approximately 0.4 m s^{-1} located over the 80-m isobath, and a weak northward flow ($v \approx 0.1$ m s^{-1}) over the innershelf off NP and NHB. The fields of σ_θ after the spinup period are characterized by isopycnals that are uplifted over the shelf and generally tilt upward toward the coast.

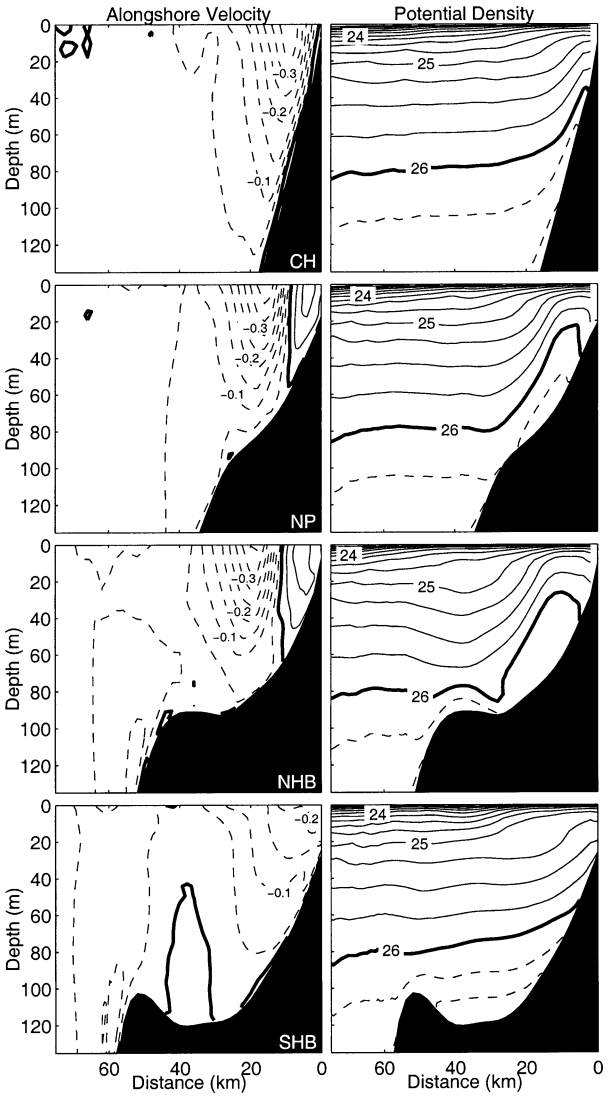

FIG. 2. Fields of v (left) and σ_θ (right) for across-shore sections off CH, NP, NHB, and SHB (denoted in Fig. 1) at the end of the 10-day spinup period. The zero v and 26-σ_θ contours are bold (contour intervals: $\Delta v = 0.05$ m s^{-1}, $\Delta \sigma_\theta = 0.25$ kg m^{-3}).

3. Model–data comparisons

The period of interest for this study is between 18 June 1999 and 17 August 1999. In Part I of this study, modeled fields were compared with a variety of observations that were obtained during the 1999 OSU NOPP field program, including time series of u, v, and θ from inshore (IS; water depth 50 m) and midshelf (MS; water depth 80 m) moorings (Boyd et al. 2000), hydrographic observations from a series of MiniBAT (Austin et al.

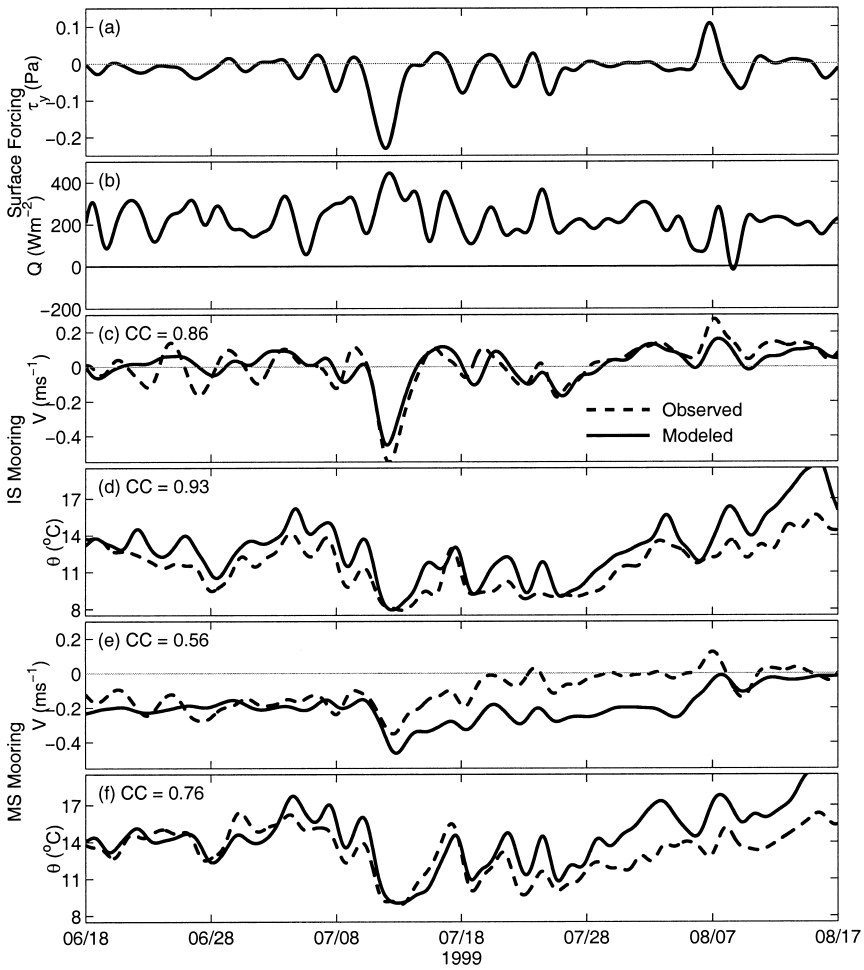

FIG. 3. Time series of (a) τ^{Sy}, (b) Q, observed (dashed) and modeled (solid) (c) V and (d) surface θ from the IS mooring, and (e) V and (f) surface θ from the MS mooring. The cross-correlation (CC) between the observed and modeled variable is presented in each panel.

2000) and SeaSoar surveys (Barth et al. 2001), and a land-based HF-radar system (e.g., Kosro et al. 1997).

Time series of modeled and observed V and surface θ from the IS and MS moorings are compared in Fig. 3. For these comparisons both the observed and modeled V is calculated by averaging v from locations where measurements were collected on the IS mooring (Fig. 1) and do not contain information from the top and bottom 10% of the water column. These comparisons demonstrate that the modeled fields are in good quantitative agreement at the IS mooring and good qualitative agreement at the MS mooring. Clearly, the agreement between the modeled and observed velocity field at the IS mooring improves after 8 July but it is not clear whether that is because the model is still spinning up until 8 July, or because the physics aren't well represented before 8 July.

For additional model–data comparisons, including comparisons with hydrographic surveys and HF radar–derived surface currents, the reader is referred to Part I of this study (Oke et al. 2002b). These comparisons demonstrate that the model results represent a substantial fraction of the observed variance for summer 1999.

4. Analysis

a. The upwelling event

The continental shelf off Oregon broadens between CH, NP, NHB, and SHB, where the shelf width is approximately 10, 30, 45, and 55 km, respectively (Fig. 1). As a result of this variation in topography, the circulation varies considerably between locations. The behavior of the coastal jet during the 12 July upwelling is demonstrated in Fig. 4 where daily averaged fields of $V(x)$ are plotted for sections off CH, NP, NHB and SHB, denoted in Fig. 1, between 7 and 18 July. Cascade Head, NP, and NHB are 40 km apart in the y direction, and SHB is 20 km south of NHB. These fields show that during the 12 July upwelling the magnitude of the coastal jet increases at all sections and the core of the coastal jet shifts onshore off CH and NP and offshore

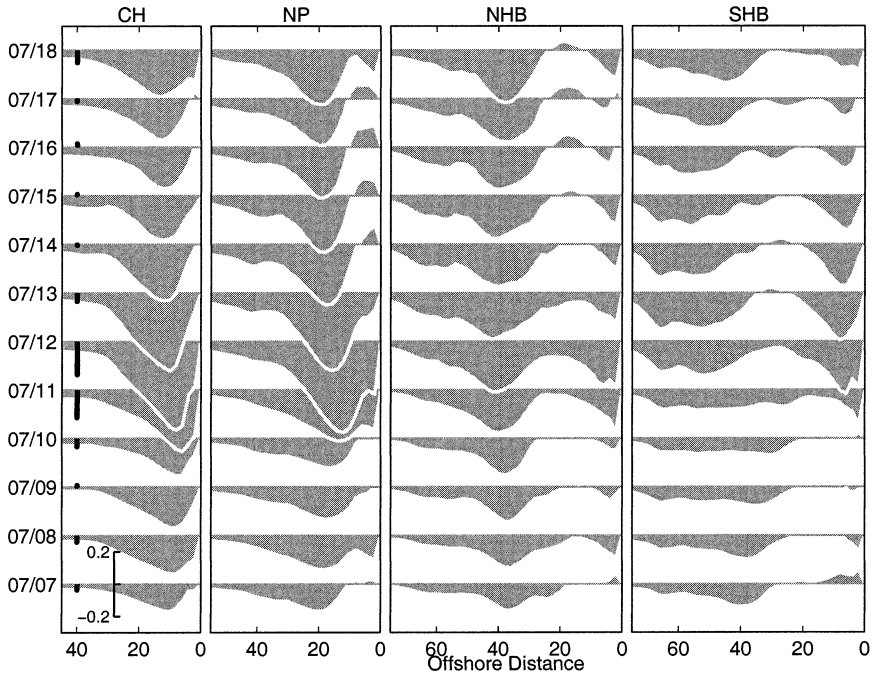

FIG. 4. Daily averaged modeled $V(x)$ off CH, NP, NHB, and SHB (left to right) during the 12 Jul upwelling event. The daily averaged τ^{Sy} is represented by the black vector on the left panel, and the scale for V in m s^{-1} and τ^{Sy} in Pa is at the bottom of the left panel.

off NHB and SHB. After the upwelling, the jet weakens and the core shifts offshore off CH and NP and onshore off NHB and SHB. Figure 4 also shows the development of the northward flow over the innershelf off NP after the 12 July upwelling between 14 and 17 July. The northward flow first appears adjacent to the coast before it broadens by a few kilometers over the next few days. Additionally, at NHB and SHB there are clearly two separate coastal jets that accelerate during the 12 July upwelling; one over the innershelf and one over the shelf break. Throughout the 12 July upwelling, however, the alongshore currents off NHB and SHB remain relatively small compared to those off CH and NP.

Daily averaged fields of v, σ_θ, and u for across-shore sections off CH, NP, NHB, and SHB, denoted in Fig. 1, on 10, 12, 14, and 16 July during an upwelling wind event, when the daily averaged τ^{Sy} is -0.03, -0.22, 0.0, and 0.03 Pa, respectively, are presented in Figs. 5, 6, 7, and 8.

1) CASCADE HEAD

The evolution of u, v, and σ_θ off CH (Fig. 5) is qualitatively consistent with the conceptual two-dimensional, wind-driven across-shore circulation. During the strong upwelling favorable winds on 12 July, there is a well defined offshore Ekman transport in u over the top 20 m of the water column and onshore flow through an upwelling bottom boundary layer (BBL) over the bottom 10–15 m of the water column. The seasonal averages and standard deviations of u and v obtained during CUE-I near NP (Huyer et al. 1978) show v with relatively strong southward currents near the bottom during spring, at the start of the upwelling season, in qualitative agreement with fields in Fig. 5. Additionally, during spring, the standard deviation of u is high near the surface and bottom, with a minimum at middepth. This is consistent with an across-shore circulation that involves fluctuations in the surface and BBLs as depicted in Fig. 5. However, by summer during CUE-I (Huyer et al. 1978) a poleward undercurrent is evident, the mean v near the bottom is more positive and the mean coastal jet does not penetrate to the bottom. Consequently, the strong near-bottom v that is necessary for a BBL flow to become established is absent and the standard deviation of u is high at middepth relative to near the bottom suggesting that the dominant across-shore circulation does not involve upwelling through a BBL consistent with conclusions from other observational studies (e.g., Huyer 1976; Halpern 1976; Smith 1981). The model results do not adequately represent a poleward undercurrent and consequently, the nature of the modeled upwelling circulation off CH may be more representative of spring conditions rather than summer conditions. The modeled BBL flow is continuous between the coast and beyond the 135-m isobath. The coastal jet accelerates towards the south, with its core shifting toward the coast around 12 July when τ^{Sy} peaks. This is consistent with the fields of $V(x)$ presented in Fig. 4. Dense water is upwelled through the BBL and the near-surface σ_θ becomes well mixed. By 14 July the

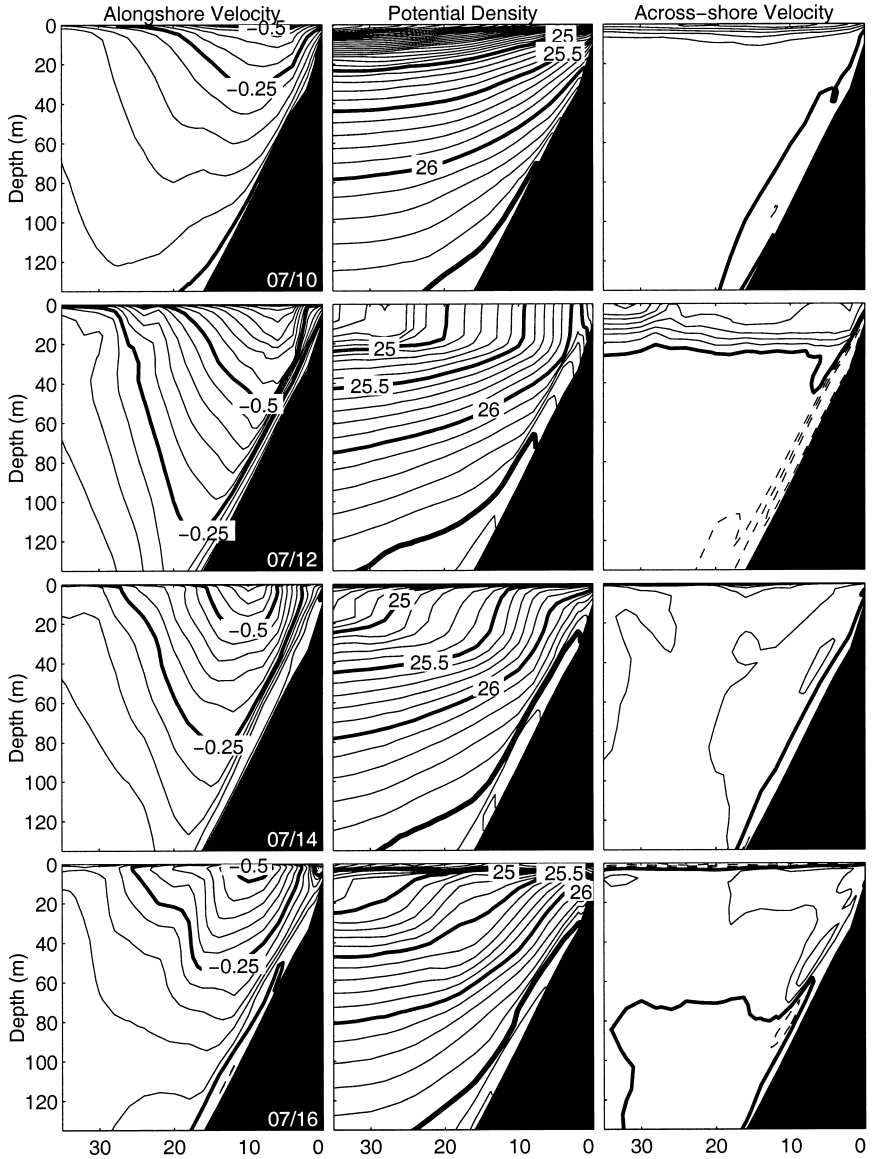

FIG. 5. Daily averaged modeled v (left), σ_θ (middle), and u (right) off Cascade Head (CH) during the 12 Jul upwelling event ($\Delta v = 0.05$ m s^{-1}, solid is southward, dashed is northward; $\Delta\sigma_\theta = 0.1$ kg m^{-3}; $\Delta u = 0.03$ m s^{-1}, solid is offshore, dashed is onshore, bold is zero). The x axis is offshore distance (km).

core of the coastal jet begins to move offshore, the extent of upwelling, evident in σ_θ, peaks, and the 26.5-σ_θ isopycnal is uplifted to shallower than the 30-m isobath. Also by 14 July, σ_θ begins to restratify near the surface in response to surface heating. By 16 July, v has weakened considerably and is approaching its preupwelled state, u is near zero, σ_θ continues to restratify near the surface, and isopycnals over the interior begin to relax toward their preupwelled state.

2) NEWPORT

The fields of v off NP (Fig. 6) show a southward acceleration between 10 and 12 July when the core of the coastal jet moves onshore. The near-surface σ_θ decreases and becomes well mixed, σ_θ becomes uplifted over the shelf, and u is offshore near the surface and over the interior and onshore in a thin BBL. In contrast to the CH section, the upwelling BBL only extends between the coast and about the 100-m isobath. By 14 July, v begins to weaken, the core of the jet moves offshore and a northward flow is generated over the innershelf. A region of dense water with $\sigma_\theta > 26.5$ appears over the midshelf. This water mass does not appear to have been upwelled from directly offshore of NP since the 26.5-σ_θ isopycnal is not continuous across the shelf. The across-shore flow is directed offshore over

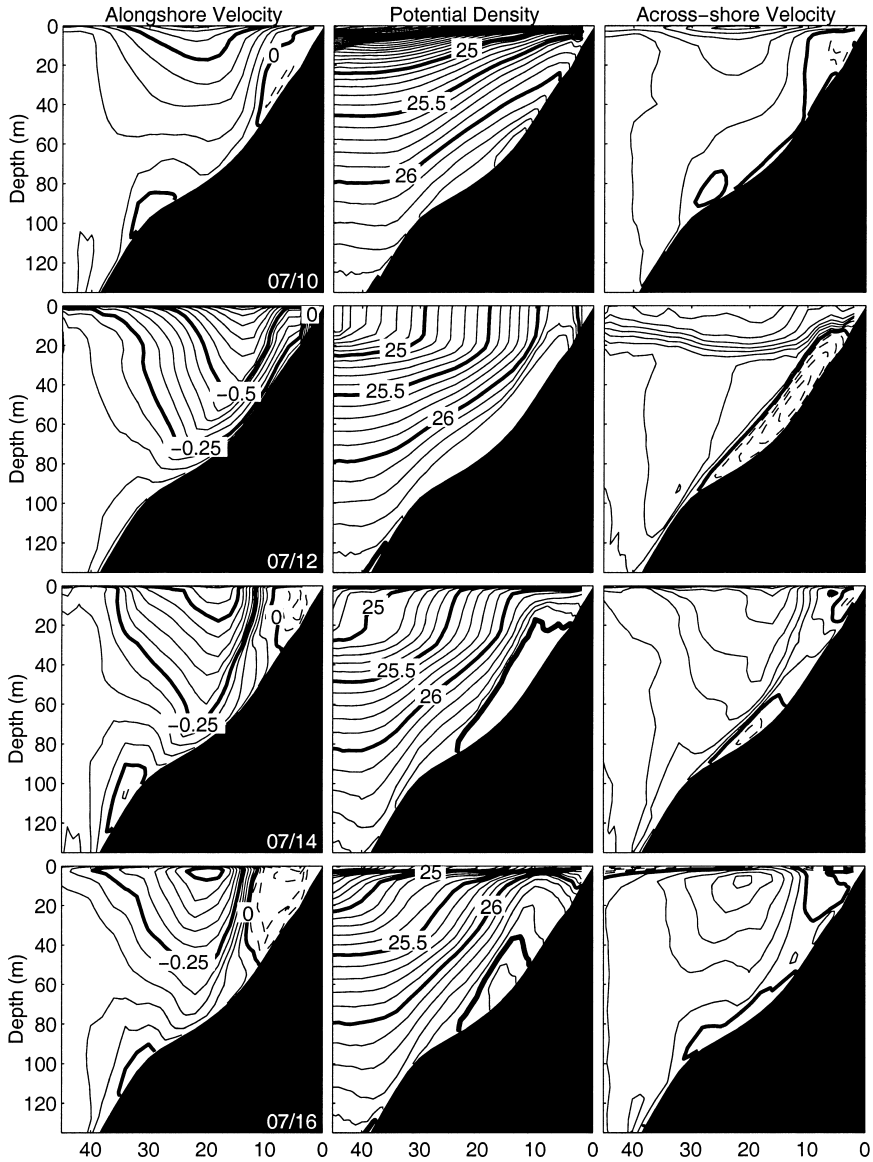

FIG. 6. As for Fig. 5 except off Newport (NP).

most of the shelf demonstrating that U is nonzero so the across-shore circulation is not two-dimensional in the x–z plane. By 16 July, the northward flow over the innershelf has strengthened and extends several kilometers farther offshore compared to 14 July. The across-shore flow remains offshore over most of the shelf and the isolated dense water mass over the midshelf is still evident and has become slightly denser. The modeled development of this isolated dense water mass over the midshelf off NP is compared to hydrographic surveys in Part I of this study with good agreement between the observed and modeled fields.

3) NORTHERN HECETA BANK

The time evolution of u, v, and σ_θ fields off NHB (Fig. 7) demonstrate that the circulation is more complicated over Heceta Bank compared to CH and NP. At each time there appears to be two distinct jets in v; one over the innershelf and one over the shelf break. This feature is also evident in Fig. 4. Between 10 and 12 July, during the strong upwelling favorable winds, the magnitude of v increases by about 0.35 m s^{-1} over the innershelf and only 0.1 m s^{-1} over the shelf break and the core of the shelf-break jet moves offshore. This is again consistent with the fields of $V(x)$ presented in Fig. 4. By 14 July, the 26-σ_θ isopycnal is uplifted to the surface over the midshelf and water with $\sigma_\theta > 26.5$ appears near the shelf break. By 16 July, v is northward over the midshelf and the doming of σ_θ over the midshelf is characteristic of a cyclonic eddy. Throughout this event the depth average of u is nonzero over the entire shelf and a large $\partial u/\partial x$ becomes evident by 14

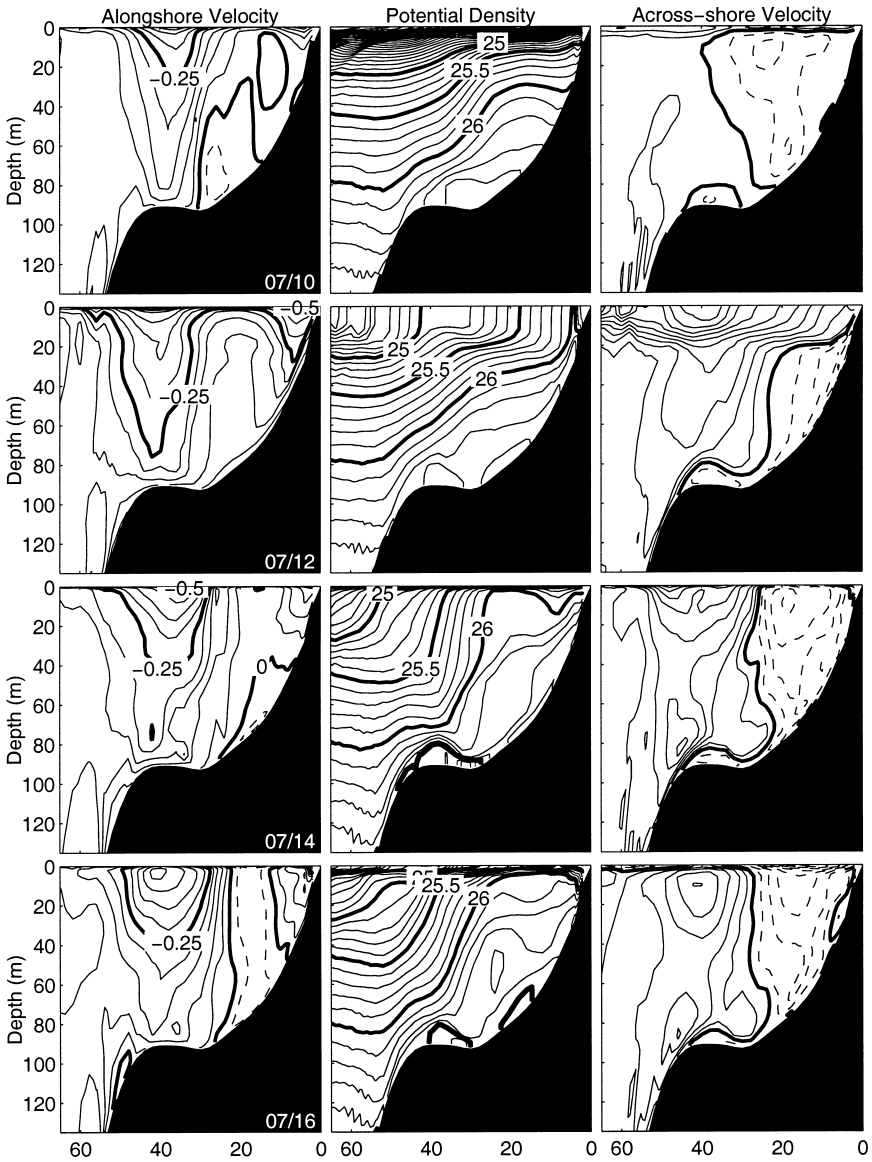

FIG. 7. As for Fig. 5 except off Northern Heceta Bank (NHB).

July. This corresponds to the period when an eddy appears to be spinning up.

4) SOUTHERN HECETA BANK

Off SHB (Fig. 8) the flow is again complicated compared to CH and NP. The differences between the circulation off SHB and NHB, described above, include the absence of the strong $\partial u/\partial x$ over the midshelf and the position of the 26-σ_θ isopycnal. This isopycnal is not uplifted as much off SHB compared to NHB but the near bottom water over the midshelf is denser compared to NHB. For each time period, water with $\sigma_\theta > 26.5$ is evident over a fairly substantial region over the midshelf. Hydrographic surveys showing similar features in σ_θ fields have previously been observed by Huyer et al. (1974).

5) WHERE DOES THE UPWELLED DENSE WATER COME FROM?

The description of the upwelling event presented above demonstrates that the flow off NP is considerably more three-dimensional than off CH during the 12 July upwelling. Additionally, the development of the isolated dense water mass over the midshelf off NP appears to be due to the alongshore advection of water that is upwelled to the north, perhaps in the vicinity of CH. This suggestion is verified by considering fields of $(u, v)^B$ and σ_θ^B where the superscript B denotes variables from

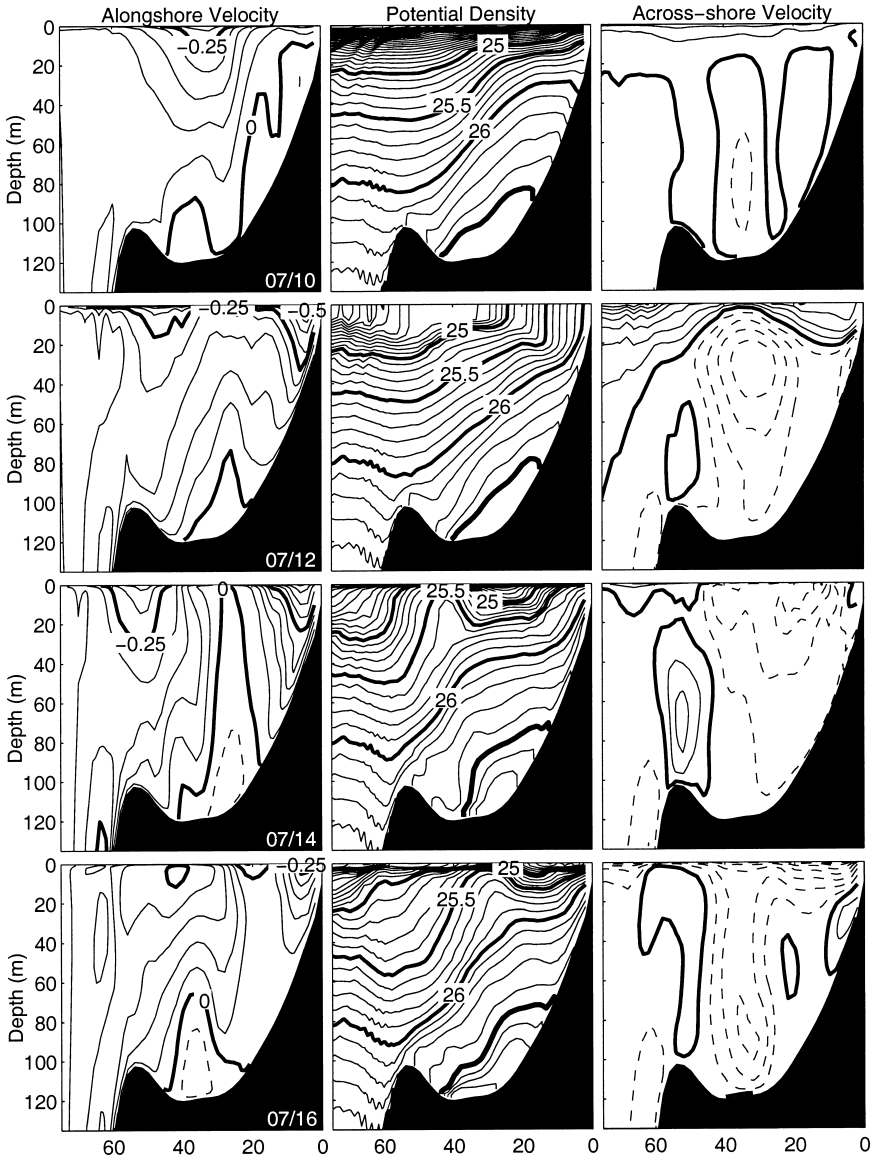

FIG. 8. As for Fig. 5 except off Southern Heceta Bank (SHB).

the bottom grid cell (Fig. 9). Fields of (U, V) and $|\tau^B|$ are also presented in Fig. 9 in order to assess the role of the coastal jet and the potential role of mixing in the development of this feature. On 12 July, $(u, v)^B$ shows a strong upwelling BBL that extends between the coast and the 200-m isobath off CH and the 100-m isobath off NP. Clearly, the BBL flow that is evident in $(u, v)^B$ on 12 and 14 July varies considerably with topography.

The sequence between 10 and 14 July shows the 26.5-σ_θ isopycnal to the north of 44.8°N being uplifted from about the 100-m isobath to less than the 50-m isobath. On 14 and 16 July, $(u, v)^B$ over the mid- and innershelf are southward in the vicinity of NP. In this region a thin tongue of water with $\sigma_\theta > 26.5$ is advected along the coast. This sequence corresponds to the development of the isolated dense water mass off NP that is evident in Fig. 6. This analysis indicates that dense water is uplifted to the north of NP and is advected southwards by near-bottom alongshore currents. The larger near-bottom (u, v) are not directly beneath the coastal jet. Along the NP section, the water over the midshelf is denser than water over the shelf break. This feature of σ_θ^B persists throughout the rest of the simulation (not shown) and does not descend down the shelf as a gravity current presumably because the flow fields around it are in near-geostrophic balance. Additionally, Fig. 9 shows water with $\sigma_\theta > 26.5$ being advected by up to 80 m in the vicinity of NHB and SHB. Fields of σ_θ^B demonstrate that this water mass is not directly connected to the dense water off NP. Rather, $(u, v)^B$ fields show that the dense water over Heceta Bank is being uplifted from the south. The fact that these water masses are not directly con-

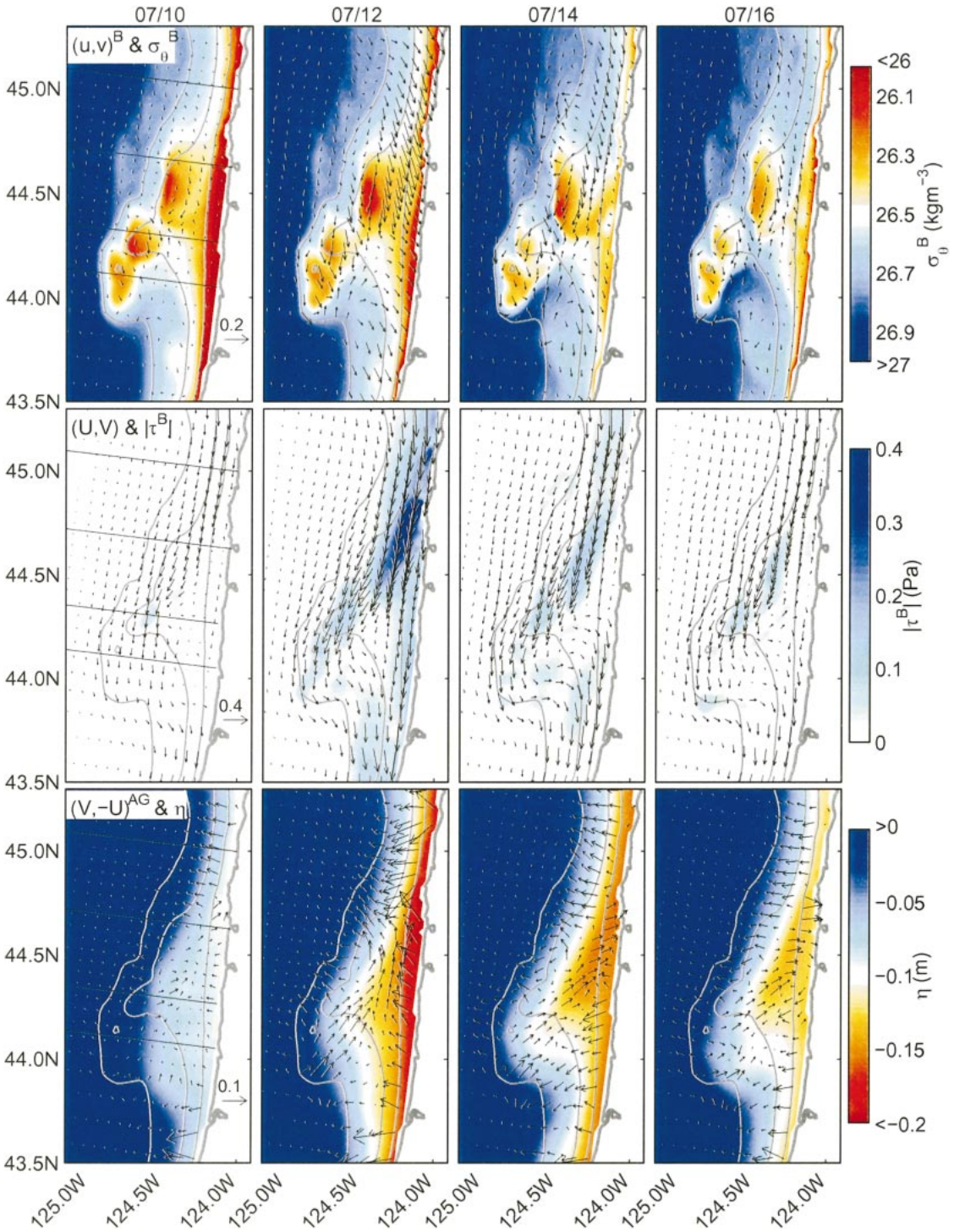

FIG. 9. Daily averaged fields of $(u, v)^B$ and σ_θ^B (top), (U, V) and $|\tau^B|$ (middle), and $(V, -U)^{AG}$ and η (bottom) showing every third vector (superscript B denotes bottom); $\sigma_\theta^B = 26.5$ is white. The across-shore sections off CH, NP, NHB, and SHB are shown on the left panels. The 50-, 100-, and 200-m isobaths are gray.

nected may have significant biological implications. The upwelled waters off NP and SHB originate in different locations and thus may have different nutrient compositions and may support different biological ecosystems. Fields of σ_θ^B after 16 July (not shown) show that these dense water masses merge after a few more days as v^B in the north continues to advect the dense water southward.

The sequence of (U, V) and $|\tau^B|$ during the 12 July upwelling (Fig. 9) shows the coastal jet accelerating over the entire shelf between 10 and 12 July with a region of larger $|\tau^B|$ generated beneath the jet off NP. On 12 July, there are two distinct jets over Heceta Bank that are also evident in Figs. 7 and 8. The strongest V over the innershelf during the upwelling is north of 44.4°N, in the region where the strong upwelling BBL flow is evident in $(u, v)^B$. The (U, V) fields remain weak over the midshelf over Heceta Bank throughout the entire event. In this region, V begins to reverse by 14 July, at which time V over the innershelf off NP is also northward. By 16 July, (U, V) qualitatively resembles its preupwelled state, although quantitatively the strength of the coastal jet on 16 July is stronger than on 10 July.

Figure 9 also shows a sequence of η and the depth-averaged ageostrophic currents U^{AG} and V^{AG} during the 12 July upwelling, where

$$U^{AG} = U - U^G, \quad \text{where } fU^G = P_y\rho_0^{-1}, \quad \text{and} \tag{4.1}$$

$$V^{AG} = V - V^G, \quad \text{where } fV^G = P_x\rho_0^{-1}, \tag{4.2}$$

where U^G and V^G are the depth-averaged geostrophic currents, f is the Coriolis parameter, P is the depth-averaged pressure, ρ_0 is a reference density, and subscripts x and y denote across-shore and alongshore derivatives, respectively. The depth-averaged horizontal momentum equations can be written symbolically as

$$(U, V)_t + \cdots = (fV - P_x\rho_0^{-1}, -fU - P_y\rho_0^{-1}) \tag{4.3}$$

$$= (fV^{AG}, -fU^{AG}), \tag{4.4}$$

where ellipses denote other terms. The components of the ageostrophic current that are relevant to the across-shore and alongshore momentum equations are V^{AG} and $-U^{AG}$, respectively. The vector field $(V, -U)^{AG}$ is therefore presented on Fig. 9. Between 12 and 16 July, $(V, -U)^{AG}$ is directed northward, and onshore between HB (124.7°W, 44°N) and NP (124.1°W, 44.65°N). This period corresponds to the time when the reversal in V is developing in the same region [see (U, V) in Fig. 9] suggesting that the dynamics that govern the flow reversal are highly ageostrophic. The fields of η for the same sequence indicates that the alongshore pressure gradient is negative in the region where $(V, -U)^{AG}$ is northward. The dynamics of this reversal are discussed in greater detail below.

To the north of NP $(V, -U)^{AG}$ is directed offshore between 10 and 16 July indicating that U^{AG} is near-zero and V^{AG} is approximately 20% of V. In this region V^{AG} is a maximum on 12 July when τ^{Sy} peaks. The sign of V^{AG} indicates that $V^G > V$ so that V is stronger to the south compared to V^G. The rms of V^{AG} off CH at 50- and 80-m depth is 0.031 and 0.042 m s^{-1}, respectively; and NP at 50- (IS mooring) and 80-m (MS mooring) depth is 0.023 and 0.016 m s^{-1}, respectively. The region where V^{AG} is large during the 12 July upwelling corresponds to a region of relatively high local Rossby number (see Fig. 13 and the discussion below) indicating that nonlinear effects are important in this region.

b. EOF analysis of the baroclinic circulation

The mean and dominant EOFs of the detrended fields of v and σ_θ for across-shore sections off CH, NP, NHB, and SHB, denoted in Fig. 1, are shown in Figs. 10 and 11, respectively. The EOFs of each section are calculated separately in order to determine to what extent the three-dimensional circulation varies together and to determine what the phase relationships are between sections. The time series of modal amplitudes of the EOFs in Figs. 10 and 11 are presented in Fig. 12. For each of these calculations, the modeled fields that are unevenly distributed on the model sigma levels are weighted according to the square root of the area of each grid cell.

1) MEAN CIRCULATION

The center of the mean southward coastal jet is located approximately 10, 20, 35, and 50 km from the coast off CH, NP, NHB, and SHB, respectively (Fig. 10). The width of the continental shelf broadens to the south in proportion to the across-shore location of the jet. The mean v fields indicate that the mean southward coastal jet is vertically sheared with a mean $\partial v/\partial z \approx 3$–$4 \times 10^{-3}$ s^{-1} off CH and NP. These characteristics of the location and vertical shear of the mean coastal jet are consistent with observations from CUE-I (off NP) and CUE-II (off CH) (Smith 1974; Kundu and Allen 1976). The mean σ_θ fields (Fig. 11) show that isopycnals are uplifted over a broader region off NHB and SHB compared to NP and CH. Isopycnals are not outcropped in the mean fields due, in part, to the effects of surface heating. The 26-σ_θ isopycnal is uplifted to 50-m depth within 10, 20, 30, and 40 km of the coast off CH, NP, NHB, and SHB, respectively. In general, isopycnals slope upward toward the coast. This is consistent with a southward geostrophic, vertically sheared alongshore current. However, over the midshelf off NHB and over the innershelf off NP, the isopycnals slope downward toward the coast. In these regions the mean v (Fig. 10) is weak (<0.05 m s^{-1}) and northward. The mean northward flow over the innershelf off NP is again consistent with results from CUE-I (Kundu and Allen 1976). Off NHB and SHB there is also a weak (<0.1 m s^{-1}), narrow, southward jet over the innershelf (Fig. 10).

2) MODE 1

The correlations between the modal amplitudes of $v(1)$, where the bracketed values refer to the EOF mode number, off CH, NP, NHB, and SHB (Fig. 12b) are all greater than 0.9 indicating that these modes typically vary together. The maximum lagged correlations between these modes and τ^{Sy} are 0.7, 0.64, 0.52, and 0.45

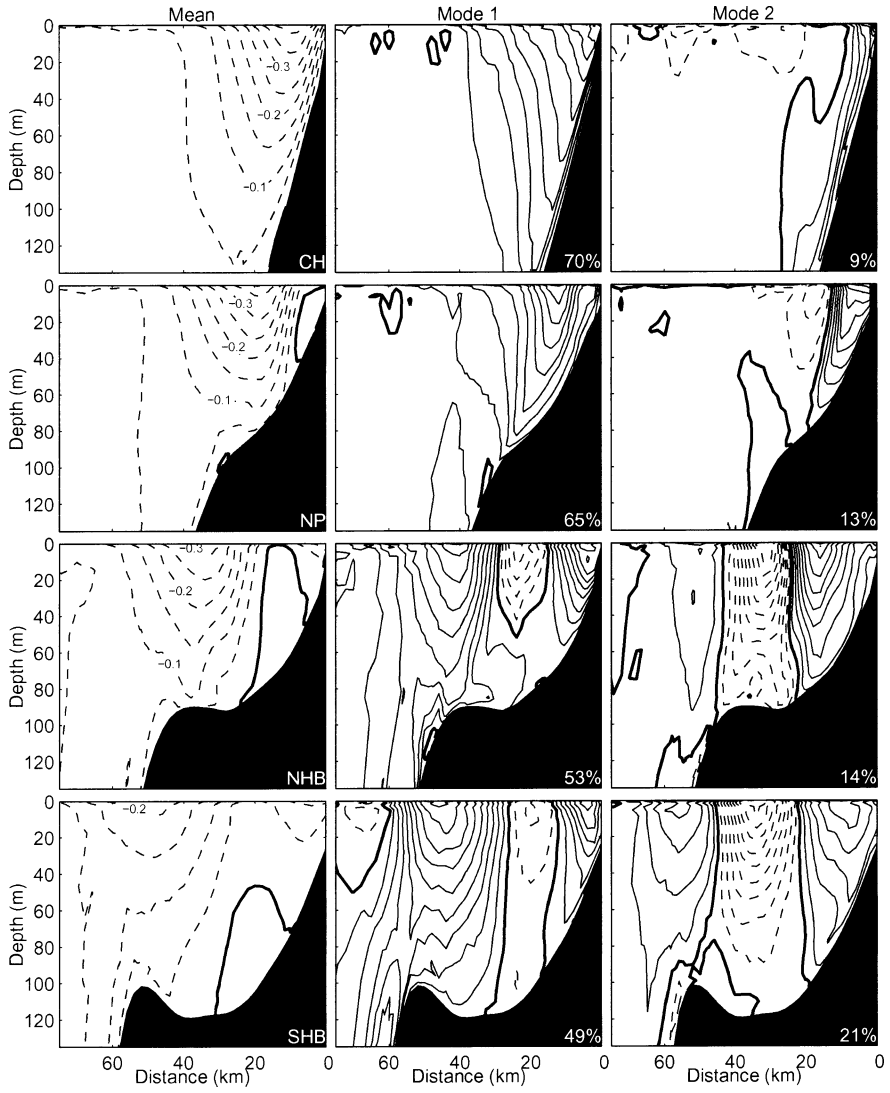

FIG. 10. Modeled mean (left) and EOFs (right) of v for across-shore sections off CH, NP, NHB, and SHB (denoted in Fig. 1). Positive, negative, and zero values are contoured with solid, dashed, and bold, solid lines, respectively. Contour intervals are 0.05 m s^{-1} for the means and 0.1 for the EOFs.

with lag times of between one and two inertial periods off CH, NP, NHB, and SHB, respectively. Additionally, the correlations between the modal amplitudes of $\sigma_\theta(1)$ off CH, NP, NHB, and SHB (Fig. 12c) are all greater than 0.87 and the maximum lagged correlations between these modes and τ^{Sy} are 0.53, 0.53, 0.44, and 0.34 with lag times of approximately two inertial periods off CH, NP, NHB, and SHB, respectively. These calculations demonstrate that $v(1)$ and $\sigma_\theta(1)$ vary together and represent responses to the wind.

The percentage of total variance explained by $v(1)$ is 70%, 65%, 53%, and 49% off CH, NP, NHB, and SHB, respectively. The calculations above show that these modes represent the dominant wind-driven modes. The trend in the percentage of total variance explained implies that the fluctuations in v are not directly linked to the wind-forcing as strongly over Heceta Bank where the continental shelf is wide compared to CH and NP. Evidently flow–topography interactions complicate the circulation in this region. The structures of $v(1)$ off CH and NP are similar (Fig. 10). Off CH, $v(1)$ represents the acceleration of a nearly barotropic coastal jet over the entire shelf and off NP, $v(1)$ represents the acceleration of a coastal jet that is nearly barotropic over the midshelf, with increased vertical shear over the inner-shelf. This is consistent with the conceptual picture of the shelf circulation off Oregon obtained from CUE-I and CUE-II (Smith 1974; Kundu and Allen 1976) that demonstrated that the mean v is vertically sheared, and that the fluctuating components of v are nearly barotropic. Additionally, the structure of $v(1)$ off CH and NP shows a maximum in the strength of the accelerating

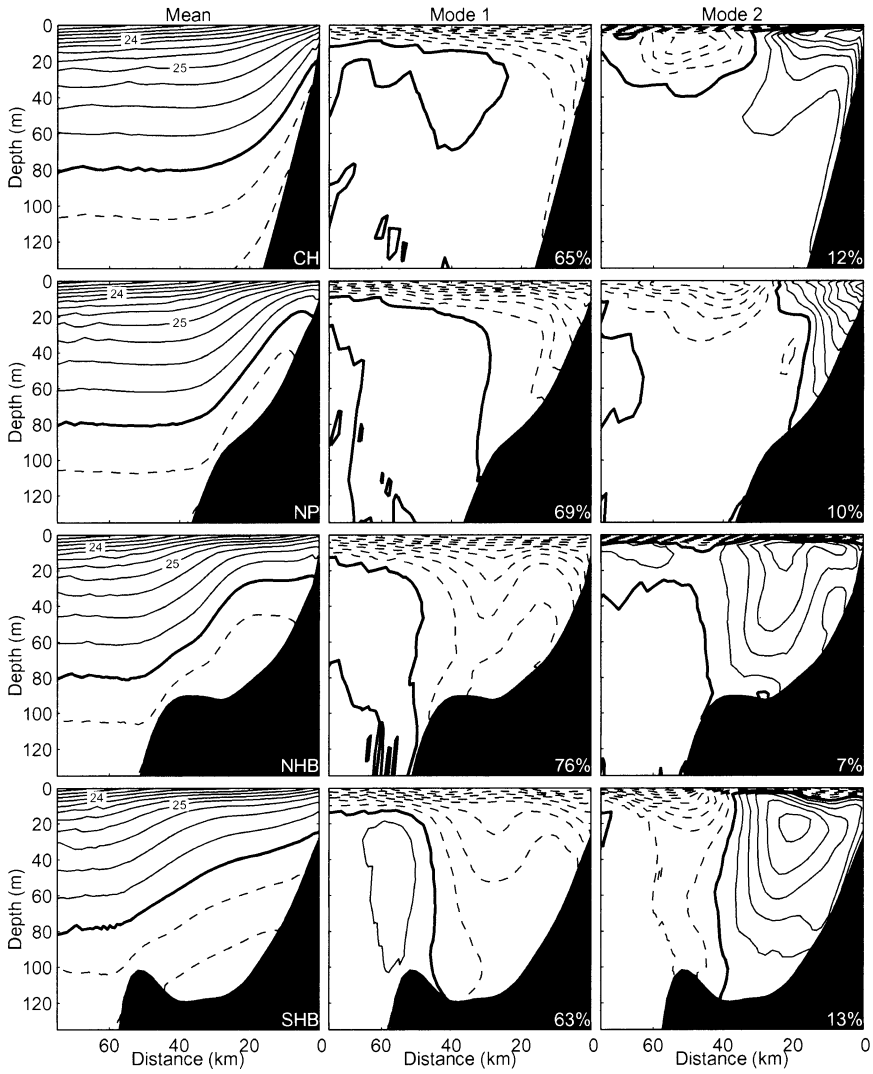

FIG. 11. Modeled mean (left) and EOFs (right) of σ_θ for across-shore sections off CH, NP, NHB, and SHB (denoted in Fig. 1). Positive, negative, and zero values are contoured with solid, dashed, and bold, solid lines, respectively, for the EOFs and the contour interval is 0.1. For the means, $\sigma_\theta = 26$ is bold; $\sigma_\theta > 26$ is dashed; $\sigma_\theta < 26$ is solid; and the contour interval is 0.25 kg m^{-3}.

jet shoreward of the maximum of the mean coastal jet, indicating that the core of the coastal jet shifts toward the coast during upwelling, and away from the coast after the upwelling favorable winds relaxes. This is consistent with the fields of $V(x)$ presented in Fig. 4.

The structure of $v(1)$ off NHB and SHB (Fig. 10) are similar to each other, but are quite different to $v(1)$ off CH and NP. The EOFs off NHB and SHB represent the acceleration of two distinct jets; one over the innershelf and one over the shelf break. There is also a weak northward acceleration over the mid-shelf during upwelling off both sections. From the time sequence of v off NHB and SHB, presented in Figs. 7 and 8; (U, V), presented in Fig. 9; and $V(x)$, presented in Fig. 4, for the 12 July upwelling this region of suggested northward acceleration really corresponds to an offshore shift of the core of the shelf break jet during upwelling. This is in contrast to the CH and NP sections where the coastal jet shifts onshore during upwelling.

The structure of $\sigma_\theta(1)$ off CH and NP indicates that upwelling off CH and NP extends between the coast and the 120- and 80-m isobaths, respectively. The offshore near-surface signature of $\sigma_\theta(1)$ is consistent with surface mixed layer dynamics where the surface mixed layer deepens during strong wind followed, when the wind is light, by restratification due to surface heating. During the mixing σ_θ increases near the surface due to entrainment of denser water from below and decreases below the mixed layer due to entrainment of lighter water from above. Off NHB and SHB, the structures of

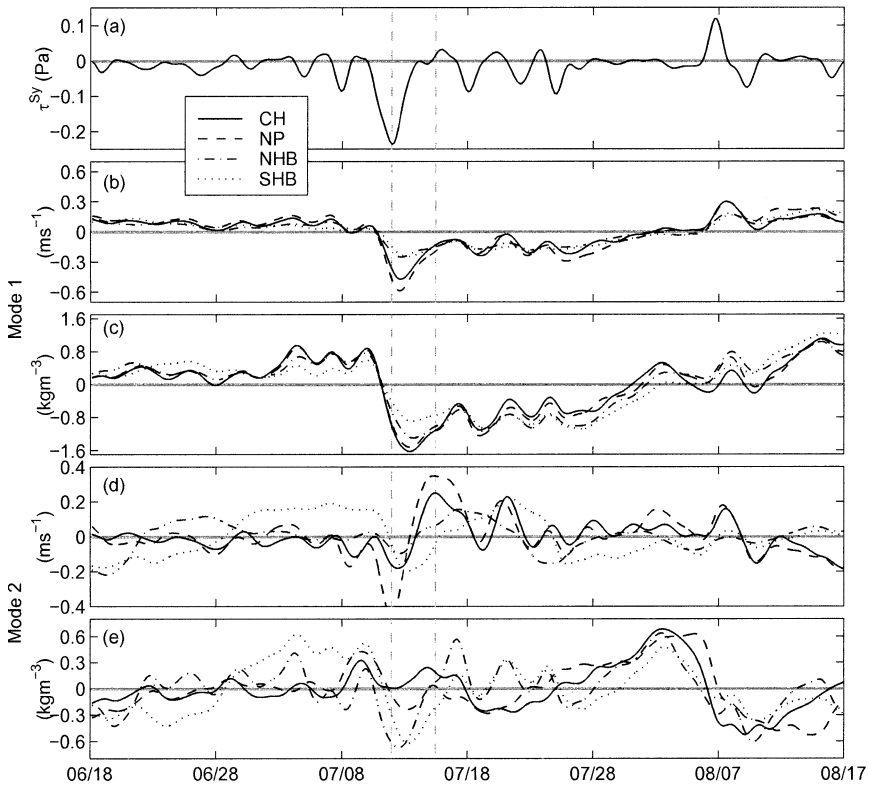

FIG. 12. Time series of (a) τ^{Sy}; (b), (c) mode-1 amplitudes; and (d), (e) mode-2 amplitudes of v and σ_θ off CH (solid), NP (dashed), NHB (dashed–dotted), and SHB (dotted). The timing of the 12 Jul upwelling and the relaxation is marked by the vertical dashed lines.

$\sigma_\theta(1)$ are similar with larger amplitude fluctuations over the midshelf and both represent fluctuations that are consistent with the development of a cold-core eddy over Heceta Bank. This is consistent with the sequences presented in Figs. 7 and 8.

3) MODE 2

The maximum lagged correlation between the modal amplitudes of $v(2)$ off CH and NP (Fig. 10) is 0.9 with CH lagging NP by half an inertial period. The most significant fluctuation of $v(2)$ off CH and NP is the negative acceleration during the 12 July upwelling and the positive acceleration after the upwelling favorable wind stops (Fig. 12d). The structures of $v(2)$ off CH and NP are similar. Both represent a southward acceleration over the inner-shelf during the 12 July upwelling and a northward acceleration over the inner-shelf during the upwelling relaxation. The negative acceleration of the modal amplitude of $v(2)$ off CH and NP during the 12 July upwelling immediately precedes the negative acceleration of $v(1)$. This is interpreted as a local response to wind and is consistent with the standard conceptual model of wind-driven upwelling where the wind-driven coastal jet accelerates first adjacent to the coast before accelerating in a broader region over the entire shelf. The positive acceleration of the modal amplitude of $v(2)$ off NP after the 12 July upwelling is interpreted as the generation of the northward flow that is also evident in Fig. 6.

The structure of $v(2)$ off SHB (Fig. 10) suggests that this mode is related to the generation of an eddy over Heceta Bank. The modal amplitude of $v(2)$ off SHB (Fig. 12d) is positive between 28 June and 12 July and is negative between 25 July and 7 August. This quasi–step-wise variability (Fig. 12d) may be related to the generation of a cyclonic eddy over Heceta Bank. This is probably associated with the eddy-like structure in the σ_θ field over SHB that is represented by $\sigma_\theta(1)$ (Fig. 11), which shows a similar step-wise variation before and after the 12 July upwelling (Fig. 12c).

c. EOF analysis of the barotropic circulation

The mean, dominant EOFs and modal amplitudes of the detrended (U, V) fields are shown in Fig. 13. Also shown in Fig. 13 is the local Rossby number $\text{Ro} = |V_x - U_y| f^{-1}$ of the mean field and of the EOF modes, using the rms amplitude for each EOF. In the regions where Ro is not small, nonlinear advection is likely to play an important role in the modeled dynamics.

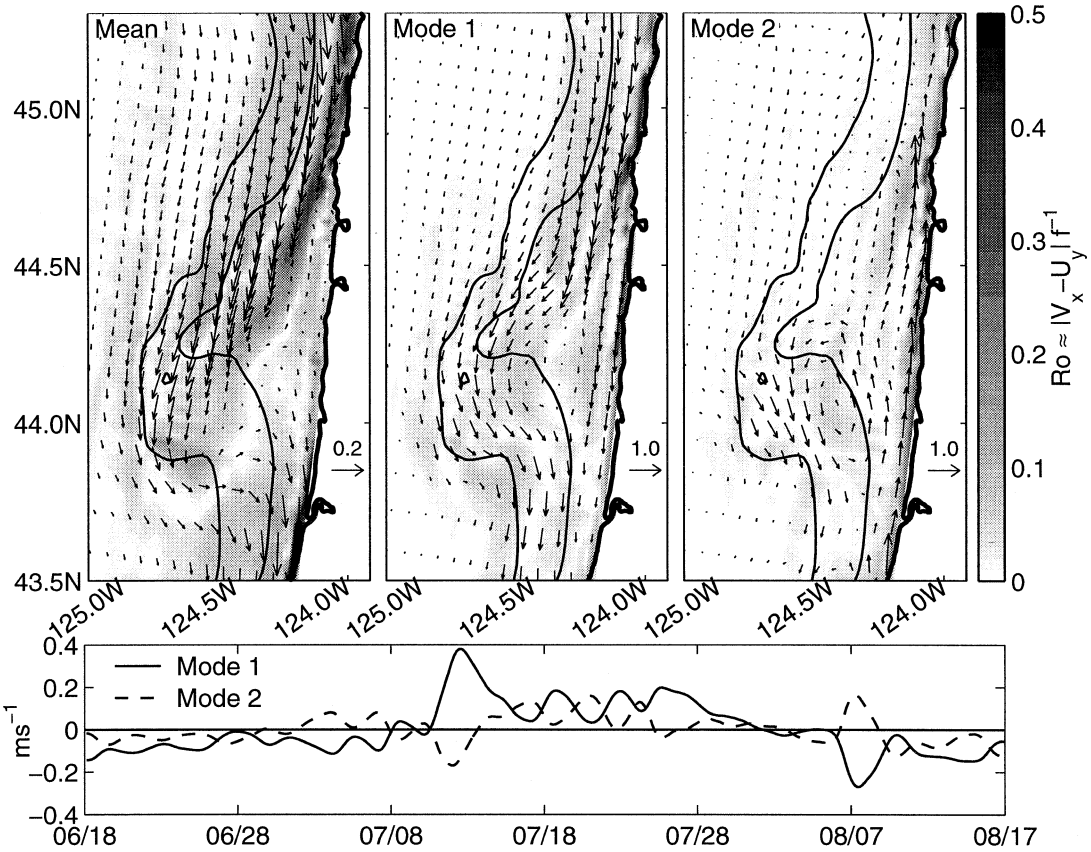

FIG. 13. The modeled mean (left) and EOFs (right) of (*U, V*), showing every fourth vector (EOF mode 1 and 2 represents 56% and 9% of the total variance, respectively); and the time series of the mode-1 (solid) and mode-2 amplitudes (bottom). The local Rossby number Ro = $|V_x - U_y| f^{-1}$ is contoured using the rms amplitude for each mode.

1) MEAN CIRCULATION

The mean (*U, V*) field (Fig. 13) shows the coastal jet to the north of HB flowing southward along isobaths. To the south of HB the currents flow onshore, realigning with the coast at around 43.7°N. The local Ro (Fig. 13) is greatest on the shoreward side of the coastal jet off NP with values around 0.5. The same calculation for the mean surface (u, v) field yields a maximum Ro $\approx$ $O(0.8)$ on the shoreward edge of the coastal jet. This region of relatively high Ro corresponds to the region where V^{AG} is relatively large (Fig. 9). The mean (*U, V*) field is similar to the fields obtained from an assimilation experiment that utilized the same model configuration for summer 1998 (Oke et al. 2002a).

2) MODE 1

The maximum lagged correlation between the amplitude of (*U, V*)(1) (Fig. 13) and τ^{Sy} is -0.7 with τ^{Sy} leading (*U, V*)(1) by 0.2 days. Clearly, this mode represents the dominant wind-driven mode. While the structure of (*U, V*)(1), representing 56% of the total variance, is similar to the mean (*U, V*) field (Fig. 13), representing fluctuations of along-isobath flow, there are some important differences. The mean (*U, V*) field shows very weak mean flow on the shoreward side of the coastal jet between 44°N and 44.5°N. In contrast (*U, V*)(1) is relatively large in this area indicating that there is a significant wind-driven response over the inner-shelf between HB and NP. Additionally, the across-shore location of the maximum in (*U, V*)(1) is on the shoreward side of the maximum of the mean flow, indicating that as the coastal jet accelerates, it also moves toward the coast. These characteristics are consistent with the fields of v(1) (Fig. 10), which shows a strong wind-driven response over the innershelf off CH, NP, NHB, and SHB.

3) MODE 2

The structure of (*U, V*)(2) (Fig. 13), representing 9% of the total modeled variance, represents the acceleration of the northward flow over the innershelf after upwelling. The maximum lagged correlation between the modal amplitudes of (*U, V*)(1) and (*U, V*)(2) is 0.56 with (*U, V*)(1) leading (*U, V*)(2) by approximately one in-

ertial period. This is consistent with the interpretation that $(U, V)(2)$ represents fluctuations associated with relaxation from upwelling. The structure of $(U, V)(2)$ also suggests it is related to the development of an eddy in the vicinity of Heceta Bank. When the amplitude of $(U, V)(2)$ is positive, as it is for a 10-day period after the 12 July upwelling, this eddy circulation is cyclonic. This eddy is probably spinning up when the coastal jet crosses f/H contours, with H increasing, during the 12 July upwelling. The water column subsequently stretches and spins up in a cyclonic fashion.

d. Analysis of the modeled dynamics

An analysis of the depth-averaged alongshore momentum equation, hereafter the V-ME, is presented in order to examine the dominant term balances of the modeled circulation. The V-ME is given by

$$\begin{aligned} \text{TENDENCY} + \quad \text{ADVECTION} \quad + \text{AGEOSTROPHIC} - \frac{\text{SURFACE}}{\text{STRESS}} + \frac{\text{BOTTOM}}{\text{STRESS}} &= 0 \\ h^{-1}[(VD)_t + \mathbf{V}\cdot\boldsymbol{\nabla}(VD) - F^y + \quad fUD + DP_y\rho_0^{-1} \quad - \quad \tau^{Sy}\rho_0^{-1} \quad + \quad \tau^{By}\rho_0^{-1}] &= 0. \end{aligned} \tag{4.5}$$

where $\boldsymbol{\nabla} = \mathbf{i}\partial/\partial x + \mathbf{j}\partial/\partial y$; $D = h + \eta$ where h is the water depth and η is the elevation; $F^y = [(2hA_mU_x)_x + (hA_m(U_y + V_x))_y]$ is the horizontal diffusion term; A_m is the horizontal diffusion coefficient; subscripts x, y, and t denote derivatives; f is the Coriolis parameter; P_y is the alongshore pressure gradient; ρ_0 is a constant reference density; and τ^{Sy} and τ^{By} are the alongshore components of the surface and bottom stress, respectively. The horizontal diffusion term does not make a significant contribution to the term balance, however it is included in the advection term for completeness. The mean of the alongshore pressure gradient and the Coriolis terms are an order of magnitude greater than the other terms indicating that the dominant balance in the V-ME (4.5) is geostrophy and that the mean fU is geostrophically balanced. This in part reflects the geostrophic balance of the alongshore current and the fact that the local alongshore direction is not necessarily aligned with the y axis. To assess the effects of the departure from geostrophic balance we consider the sum of the alongshore pressure gradient and the Coriolis terms in an ageostrophic term to identify when and where the flow becomes significantly ageostrophic.

The mean, dominant EOFs and modal amplitudes of the terms in the V-ME (4.5) are shown in Fig. 14. This analysis is performed by constructing an $N \times K$ matrix ψ, where N is the number of points in time and K is the number horizontal grid points multiplied by the number of terms in the V-ME ($K = 69 \times 114 \times 5$). The columns of ψ represent time series of each term at each horizontal grid location. An eigenvalue decomposition of the covariance matrix of ψ, with the temporal means subtracted, is performed to obtain the EOFs and EOF amplitudes. The EOFs are normalized by their largest value and the appropriate elements for each term at each grid location is extracted. The normalized EOFs of the terms sum to zero and are therefore considered to represent balanced modes of the terms in the V-ME (4.5).

Also shown in Fig. 14 are time series of observed and modeled V at the IS mooring location and V derived from EOF modes. The time series of V derived from EOF modes are reconstructed by multiplying the modal amplitude and the EOF values for the time derivative at the IS location. This is done using just the mean and V-ME(1), denoted as $\int V_t(1)\,dt$, and using the mean, V-ME(1) and V-ME(2), denoted as $\int V_t(1) + V_t(2)\,dt$. These tendencies are then integrated over time to obtain a time series of V that is represented by the modes. This reconstruction is plotted in Fig. 14d and is compared to the observed and modeled V from the IS mooring. Clearly, V-ME(1) is dominated by the southward acceleration during the 12 July upwelling. The relaxation of V after this event is not represented by V-ME(1), because it is dominated by negative tendencies. Fluctuations of V-ME(2) represent the relaxation from upwelling. The sum of V-ME(1) and V-ME(2) does not totally represent the northward flow that is evident in the full modeled and observed V after the 12 July upwelling. The dynamics of this reversal are analyzed separately below.

1) MEAN BALANCE

The mean fields in the V-ME (4.5) (Fig. 14a) show that the advection, ageostrophic, surface stress, and bottom stress terms are all important for mean dynamical balance over the continental shelf off Oregon. The dominant mean ageostrophic balance is between the advection and the ageostrophic terms. The mean surface stress is important over the innershelf. To the north of NP the surface stress is balanced, in part, by bottom stress, but to the south of NP the mean surface and bottom stresses are clearly not balanced. In that region the surface stress is balanced by a combination of the advection and ageostrophic terms. The mean bottom stress is important between 44.4° and 44.6°N over the midshelf where the mean (U, V) field in Fig. 13 starts to flow offshore and where Ro has a local maximum (Fig. 13). This bottom stress is balanced by a combination of surface stress and advection.

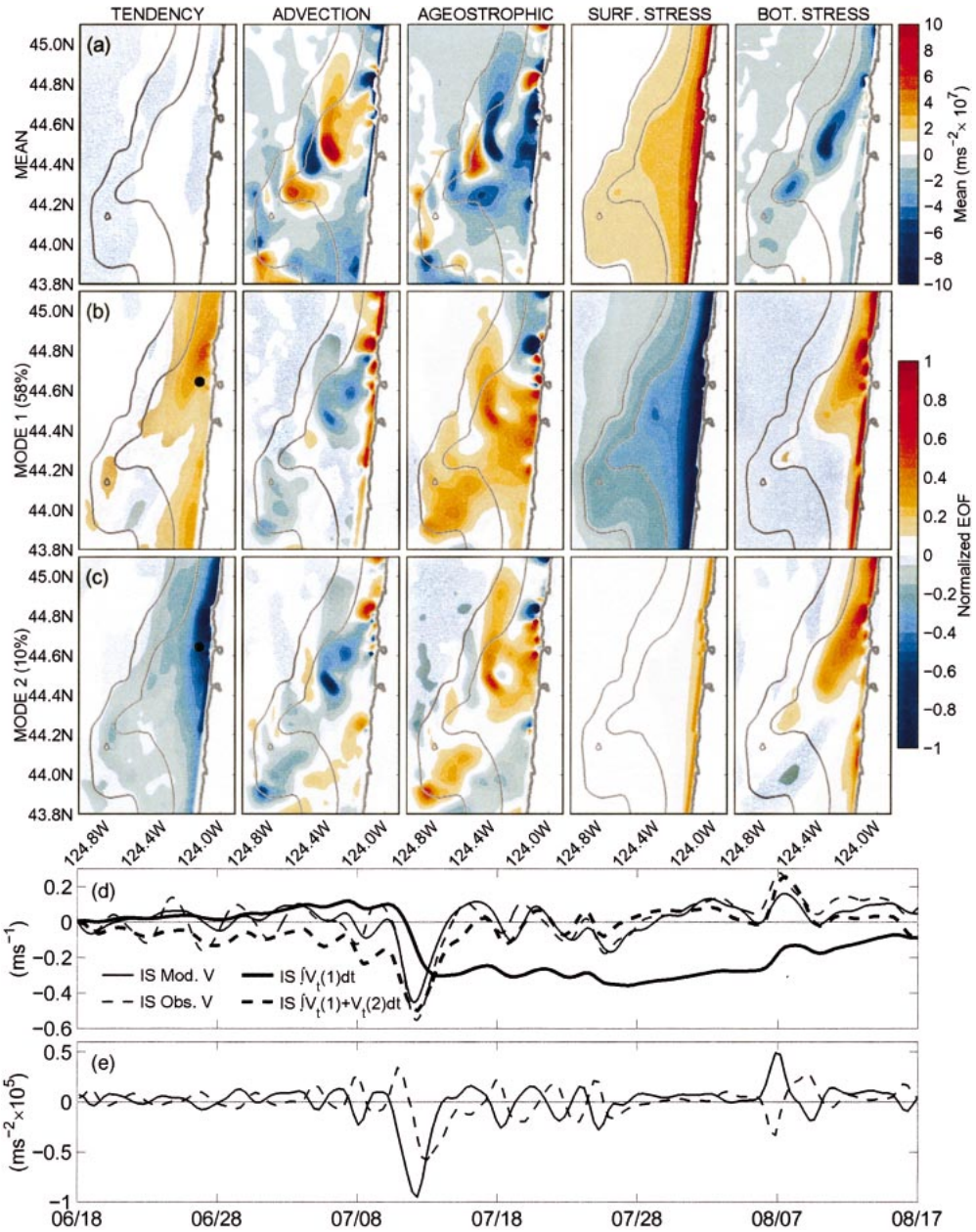

FIG. 14. (a) Mean, (b) mode-1, and (c) mode-2 normalized EOFs from the *V*-ME, and time series of (d) observed, modeled and reconstructed *V* from the IS mooring location [denoted in (b) and (c) by ●], and (e) mode 1 (solid) and mode 2 (dashed) modal amplitudes. The time series of reconstructed *V* are the time integrals of the tendency represented by the mean and mode 1 [$\int V_t(1)\,dt$] and the mean and mode 1 and 2 [$\int V_t(1) + V_t(2)\,dt$] at the IS mooring location.

2) MODE 1

As demonstrated by the reconstruction of *V* using *V*-ME(1) and the dominance of the surface stress term in this mode, *V*-ME(1) represents the dynamical balances associated with wind-driven upwelling. The amplitude of *V*-ME(1) becomes more negative during the 12 July upwelling and during the weak upwelling pulses that follow. These fluctuations correspond to a negative increase in the tendency term (southward acceleration), a positive increase in the surface stress (upwelling favorable) and a negative increase in the bottom stress term (opposing the surface stress). To the south (north) off NP during upwelling the ageostrophic term becomes increasingly negative (positive) with values of up to 10^{-5} m s^{-2}; two orders of magnitude greater than the

mean values of the ageostrophic term. In this region the ageostrophic term is the dominant term that balances the surface stress. The ageostrophic term increases in magnitude when the Coriolis and pressure gradient terms become unbalanced.

3) MODE 2

The northward acceleration of *V*-ME(2) after the 12 July upwelling (Fig. 14e) represents the dynamical balances associated with the relaxation of the coastal jet after upwelling. The main differences between *V*-ME(1) and *V*-ME(2) are in the tendency, surface stress, and bottom stress terms while the structure of the advection and the ageostrophic terms do not vary significantly. These differences are sufficient to make *V*-ME(1) and *V*-ME(2) orthogonal. When the amplitude of *V*-ME(2) is negative the tendency is positive, accelerating *V* to the north. The only terms that could balance the tendency near NP in *V*-ME(2) are the bottom stress and ageostrophic terms because advection has the wrong sign and the surface stress is too weak. The similarities between the fields of bottom stress in *V*-ME(2) and the tendency in *V*-ME(1) suggest that bottom stress is acting to retard the flow in the locations where it was accelerated during the upwelling. Additionally, to the south of NP over the innershelf the ageostrophic term is negative, representing either a negative ageostrophic alongshore pressure gradient, or an ageostrophic offshore flow.

As noted above, the flow becomes increasingly ageostrophic during upwelling. The similarities between the ageostrophic fields in *V*-ME(1) and *V*-ME(2) indicate that the large ageostrophic term, that partially balances the surface stress during upwelling [*V*-ME(1)], is the dominant term balancing the tendency [*V*-ME(2)] between 44.2° and 44.6°N over the innershelf.

4) ANALYSIS OF THE *V*-ME AT THE IS MOORING

Time series of the modeled and observed *U* and *V* and the modeled terms in the *V*-ME (4.5) during the 12 July upwelling are shown in Fig. 15. As demonstrated in section 2 and Fig. 15 the modeled and observed *U* and *V* are in good quantitative agreement at the IS mooring, giving us confidence in the validity of the modeled dynamical balances. Time series of *U* are multiplied by three in order to show the details of the fluctuations. A close comparison between the modeled *U* and *fUD* show some differences in the fluctuations. This is because both the observed and modeled *U* and *V* are calculated by averaging *u* and υ from locations where measurements were collected on the IS mooring (Fig. 1) and do not contain information from the top and bottom 10% of the water column.

All terms are plotted for values on the left-hand-side of the *V*-ME (4.5). During the 12 July upwelling the tendency is approximately balanced by the imbalance

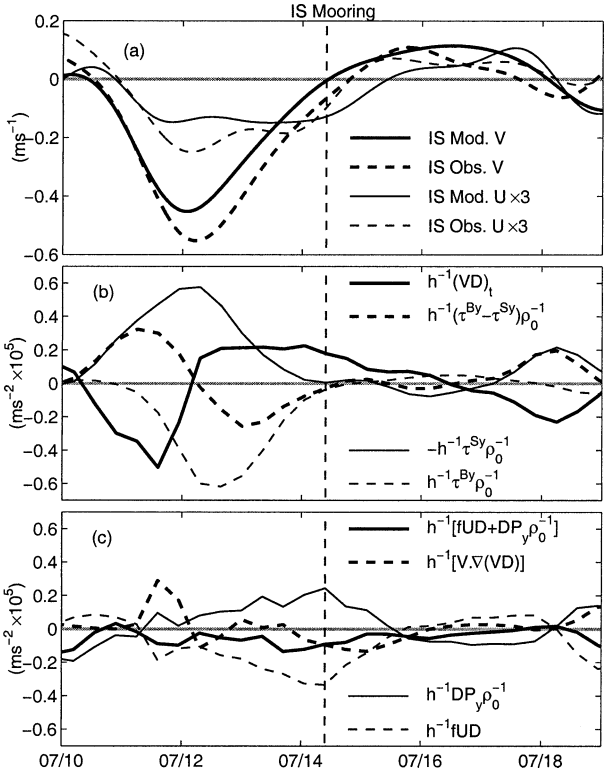

FIG. 15. Time series of (a) modeled and observed $U \times 3$ and *V* and (b), (c) terms in the *V*-ME for the 12 Jul upwelling at the IS mooring location. All terms are for values on the left-hand side of the *V*-ME. The vertical dashed line denotes the time of the reversal of the modeled *V* at the IS mooring.

between τ^{Sy} and τ^{By}. This balance is maintained until τ^{Sy}, τ^{By}, and *V* approach zero. Just before τ^{Sy}, τ^{By}, and *V* become zero the Coriolis and advection terms (Fig. 15c) increase in magnitude. The increase in the Coriolis term corresponds to an increased ageostrophic, barotropic across-shore flow, during which time there is a corresponding positive increase in the tendency. Once *V* reaches zero the tendency remains positive and is not balanced by either τ^{Sy} or τ^{By}. The ageostrophic term decreases and the advection term becomes more negative, balancing the persistent positive tendency. At the time of the reversal the advection term $UV_x + VV_y < 0$ (ignoring variations in *D*); $V = 0$; and so $VV_y = 0$. The term $fU < 0$ and so $V_x > 0$, corresponding to a weaker southward (or stronger northward) flow near the coast. Therefore, at the time of the reversal, the balance in the *V*-ME (4.5) at the IS mooring location is

$$V_t + UV_x + fU_{AG} = 0, \tag{4.6}$$

where fU_{AG} is the ageostrophic component of *fU*. After the reversal fU_{AG} approaches zero and advection balances the persistent northward tendency. We interpret this increase in UV_x to be effecting the across-shore adjustment of the coastal jet that is evident in $\upsilon(2)$ (Fig. 10) and to be advecting northward momentum offshore, resulting in the northward tendency. Advection is a

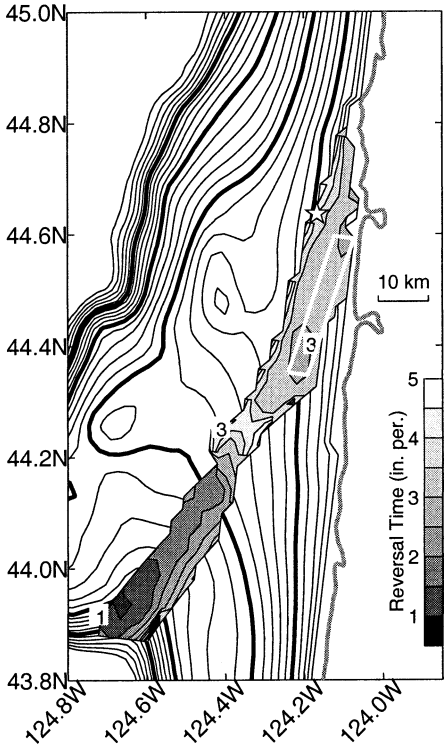

FIG. 16. The reversal time of V relative to the time of the peak of τ^{Sy} during the 12 Jul upwelling for each location. Where the reversal time is not shown, V does not reverse. The topography is contoured at intervals of 10 m, and the 50-, 100-, 150-, and 200-m isobaths are bold. The location of the IS mooring is denoted by the star and the generation site for the location of the IS mooring is outlined in white.

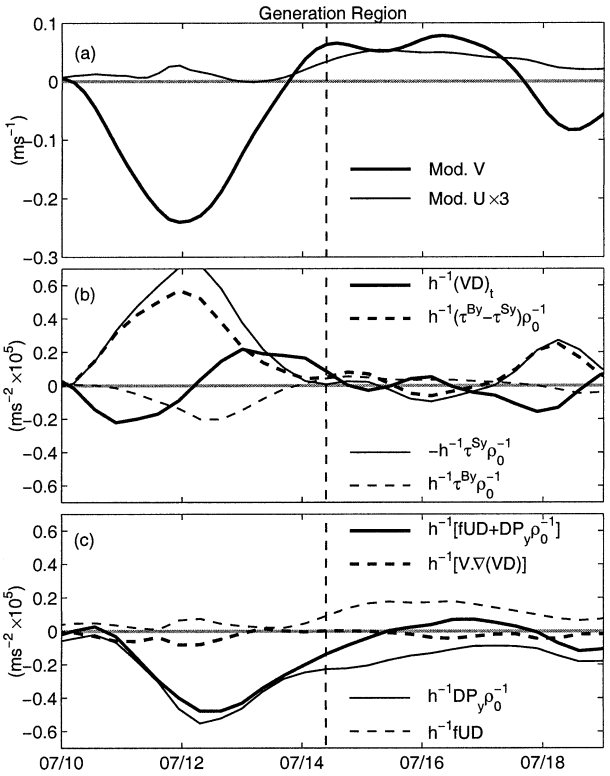

FIG. 17. Time series of area-averaged (a) modeled $U \times 3$ and V and (b), (c) terms in the V-ME for the 12 Jul upwelling for the generation region (denoted in Fig. 16). All terms are for values on the left-hand side of the V-ME. The vertical dashed line denotes the time of the reversal of V at the IS mooring.

transfer of momentum and so the question now becomes, how and where is the northward momentum generated?

During the 12 July upwelling, V is southward throughout the entire domain (Fig. 9). In order to address where the northward momentum is generated we calculate the time interval after 12 July, relative to the time of the peak in the magnitude of τ^{Sy}, when V first becomes northward for every location (Fig. 16). This demonstrates that V first flows northwards over Heceta Bank, located approximately 90 km away from the IS mooring. The region where V reverses corresponds to the region where the depth-averaged ageostrophic currents became large and northward during the 12 July upwelling presented in Figure 9. The time delay between the reversal over Heceta Bank and the IS mooring is not monotonic between the two regions, indicating that the northward momentum generated over Heceta Bank is not simply advected to the IS mooring location. Additionally, these locations are too far apart for advection to transfer the momentum over 4–5 inertial periods as suggested in Fig. 16. The region over the innershelf to the south of Newport, outlined in white in Fig. 16, is a location where northward flow develops within three inertial periods of the 12 July upwelling peak. This region is the site where the northward momentum is generated before being advected to the IS mooring location. The speed of advection required to transfer this northward momentum to the IS mooring location is 0.04–0.25 m s^{-1}. This description is consistent with the modeled circulation.

A detailed analysis of the area-averaged terms in the V-ME (4.5) for the generation site denoted in Fig. 16, is presented in Fig. 17. This analysis clearly shows that during the upwelling favorable winds the surface stress is primarily balanced by a negative alongshore pressure gradient. Notably, bottom friction is small compared to the IS mooring because this region is shoreward of the coastal jet, so bottom currents and hence the bottom stresses are small. When the wind stops, the alongshore pressure gradient balances a northward tendency, effecting the reversal and acting to drive the alongshore currents to the north. As the northward flow becomes established the alongshore pressure gradient relaxes and becomes balanced by the Coriolis term, positive fUD. After this adjustment the flow is approximately geostrophic and the northward V persists for several days.

5. Summary

Sixty-day simulations of the sub-inertial continental shelf circulation off Oregon are performed for a hindcast

study of summer 1999. In Part I of this study (Oke et al. 2002b) the model results are shown to compare favorably with in situ currents, HF radar–derived surface currents and hydrographic measurements obtained from an array of moored instruments and field surveys. The correlations between observed and modeled currents and temperatures in water depths of 50 m are in excess of 0.8.

The detailed analysis of the modeled flow fields provides a complete synoptic description of the three-dimensional, time-varying continental shelf circulation off Oregon for summer 1999. The circulation is clearly wind-driven with significant alongshore variations caused by the alongshore variations in topography. In the region of the coast where the alongshore topographic variations are small, the upwelling circulation is qualitatively consistent with the standard conceptual two-dimensional across-shore circulation. This is in agreement with observations off Oregon during spring (Huyer et al. 1978). In the regions where the alongshore topographic variations are greater, the upwelling circulation is highly three-dimensional. The analysis of the baroclinic fields for sections off CH, NP, NHB, and SHB demonstrates that the response to upwelling favorable winds involving acceleration of a southward coastal jet, occurs in unison at all four sections. The percentage of total variance explained by the dominant wind-driven mode at each section and the correlation between the wind and the mode-1 amplitudes for each section show that the circulation over Heceta Bank has a weaker connection with direct wind forcing than the circulation off CH and NP. Over Heceta Bank there are two distinct southward jets that accelerate during upwelling favorable winds; one over the innershelf and one over the shelf break. During upwelling the coastal jet moves toward the coast over the narrow continental shelf off CH and NP, while the component of the jet that is located over Heceta Bank moves seaward. The analysis of the barotropic response demonstrates that the dominant wind-driven flow is along-isobath, with large fluctuations over the innershelf.

It is demonstrated that the upwelled water that is found over the midshelf off Newport is upwelled to the north, and is advected southward beneath the coastal jet. Additionally, upwelled water over Heceta Bank is advected northward from a different location to the south.

The analysis of the term balances in the *V*-ME (4.5) shows that in general the flow becomes increasingly ageostrophic during upwelling. During relaxation from upwelling, bottom stress plays an important role acting to retard the alongshore flow over the inner- and midshelf to the north of 44.4°N. To the south of 44.4°N, the alongshore flow is retarded by a negative alongshore pressure gradient.

The dynamical balances over the innershelf are divided into two regimes; in the coastal jet and inshore of the coastal jet. In the coastal jet V_t is large and is driven by the difference between the surface and bottom stresses during upwelling:

$$(VD)_t = (\tau^{Sy} - \tau^{By})\rho_0^{-1}. \quad (5.1)$$

Inshore of the coastal jet V_t is small and is driven by the difference between the surface stress and a negative alongshore pressure gradient during upwelling:

$$(VD)_t = (\tau^{Sy} - DP_y)\rho_0^{-1}. \quad (5.2)$$

When the wind stress reduces to zero, V_t is balanced by a negative pressure gradient

$$(VD)_t = -DP_y\rho_0^{-1}, \quad (5.3)$$

and a northward flow is generated. After the northward flow is generated, the alongshore pressure gradient relaxes and the flow becomes geostrophic. The northward flow persists for several days. A region to the south of Newport over the innershelf is identified as the region where the northward momentum is initially generated following the sequence of term balances outlined above. This northward momentum is subsequently advected by the currents and a northward flow is generated at the IS mooring through the approximate balance,

$$V_t + UV_x + fU_{AG} = 0. \quad (5.4)$$

The generation of this northward flow after upwelling is frequently observed off Newport (e.g., Huyer et al. 1974; Kundu and Allen 1976), but the mechanism by which this northward flow is generated has not been previously explained.

Acknowledgments. This research was supported primarily by the National Oceanographic Partnership Program (NOPP) through ONR Grant N00014-98-1-0787. Support was also provided by the ONR Ocean Modeling and Prediction Program through Grant N00014-98-1-0043 and by an ONR DURIP Grant N00014-99-1-0773. The authors gratefully acknowledge Murray Levine, Mike Kosro, and Tim Boyd for providing observations used in this study.

REFERENCES

Allen, J. S., P. A. Newberger, and J. Federiuk, 1995: Upwelling circulation on the Oregon continental shelf. Part I: Response to idealized forcing. *J. Phys. Oceanogr.*, **25,** 1843–1866.

Austin, J. A., J. A. Barth, and S. D. Pierce, 2000: Small-boat hydrographic surveys of the Oregon mid- to inner-shelf. Oregon State University Data Rep. 178, 00-2, 99 pp.

Barth, J. A., R. O'Malley, A. Y. Erofeev, J. Fleischbein, S. D. Pierce, and P. M. Kosro, 2001: SeaSoar CTD observations from the central Oregon shelf, W9907C, 13–31 July 1999. Oregon State University Data Report 184, 01-5, 355 pp.

Blumberg, A. F., and G. L. Mellor, 1987: A description of a three-dimensional coastal ocean circulation model. *Three-Dimensional Coastal Ocean Models,* N. Heaps, Ed., Vol. 4, Amer. Geophys. Union, 1–16.

Boyd, T., M. D. Levine, P. M. Kosro, and S. R. Gard, 2000: Mooring observations from the Oregon continental shelf. Oregon State University Data Rep. 177, 00-1, 216 pp.

Chapman, D. C., 1985: Numerical treatment of cross-shelf open

boundaries in a barotropic coastal ocean model. *J. Phys. Oceanogr.*, **15,** 1060–1075.

Gan, J., and J. S. Allen, 2002: A modeling study of shelf circulation off northern California in the region of the Coastal Ocean Dynamics Experiment. Part 1: Response to relaxation of upwelling wind. *J. Geophys. Res.*, in press.

Halpern, D., 1976: Structure of a coastal upwelling event observed off Oregon during July 1973. *Deep-Sea Res.*, **23,** 495–508.

Huyer, A., 1976: A comparison of upwelling events in two locations: Oregon and northwest Africa. *J. Mar. Res.*, **34,** 531–546.

——, R. L. Smith, and R. D. Pillsbury, 1974: Observations in a coastal upwelling region during a period of variable winds (Oregon coast, July 1972). *Tethys*, **6,** 391–404.

——, ——, and E. J. C. Sobey, 1978: Seasonal differences in low-frequency current fluctuations over the Oregon continental shelf. *J. Geophys. Res.*, **83,** 5077–5089.

Kosro, P. M., J. A. Barth, and P. T. Strub, 1997: The coastal jet: Observations of surface currents along the Oregon Continental Shelf from HF radar. *Oceanography*, **10,** 53–56.

Kundu P. K., and J. S. Allen, 1976: Some three-dimensional characteristics of low-frequency current fluctuations near the Oregon coast. *J. Phys. Oceanogr.*, **6,** 181–199.

Mellor, G. L., and T. Yamada, 1982: Development of a turbulence closure model for geophysical fluid problems. *Rev. Geophys. Space Phys.*, **20,** 851–875.

Oke, P. R., J. S. Allen, R. N. Miller, G. D. Egbert, and P. M. Kosro, 2002a: Assimilation of surface velocity data into a primitive equation coastal ocean model. *J. Geophys. Res.*, in press.

——, and Coauthors, 2002b: A modeling study of the three-dimensional continental shelf circulation off Oregon. Part I: Model–data comparisons. *J. Phys. Oceanogr.*, **32,** 1360–1382.

Smagorinsky, J., 1963: General circulation experiments with primitive equations. I. The basic experiment. *Mon. Wea. Rev.*, **91,** 99–164.

Smith, R. L., 1974: A description of current, wind, and sea level variations during coastal upwelling off the Oregon coast, July–August 1972. *J. Geophys. Res.*, **79,** 435–443.

——, 1981: A comparison of the structure and variability of the flow field in three coastal upwelling regions: Oregon, northwest Africa, and Peru. *Coastal Upwelling*, F. Richards, Ed., Coastal and Estuarine Sciences Series, Vol. 1, Amer. Geophys. Union, 107–118.

Stevenson, M. R., R. W. Garvine, and B. Wyatt, 1974: Lagrangian measurements in a coastal upwelling zone off Oregon. *J. Phys. Oceanogr.*, **4,** 321–336.